AIMS Materials Science, 2(4), 484-496.
DOI: 10.3934/matersci.2015.4.484
Received date 27 May 2015,
Accepted date 16 November 2015,
Published date 19 November 2015

http://www.aimspress.com/

Research article

Direct observations of ferromagnetic and antiferromagnetic domains in Pt/Co/Cr_2O_3/Pt perpendicular exchange biased film

Yu Shiratsuchi [1,*], Yoshinori Kotani [2], Saori Yoshida [1], Yasunori Yoshikawa [1], Kentaro Toyoki [1], Atsushi Kobane [1], Ryoichi Nakatani [1], and Tetsuya Nakamura [2]

[1] Department of Materials Science and Engineering, Graduate School of Engineering, Osaka University, 2-1 Yamadaoka, Suita, Osaka 5650871, Japan
[2] Japan Synchrotron Radiation Research Institute (JASRI)/SPring-8, 1-1-1, Kouto, Sayo, Hyogo 6795198, Japan

* **Correspondence:** Email: shiratsuchi@mat.eng.osaka-u.ac.jp; Tel/Fax: +81-6-6879-7489.

Abstract: By using focused soft X-rays, magnetic domain imaging based on X-ray magnetic circular dichroism (XMCD) measurements was performed on a Pt/Co/Cr_2O_3/Pt film that exhibits both perpendicular magnetic anisotropy and perpendicular exchange anisotropy. In the AC-demagnetized state, spatial distributions of the XMCD corresponding to the magnetic domains were clearly observed. In particular, ferromagnetic and antiferromagnetic magnetic domains were separately observed by tuning the photon energy to either the ferromagnetic Co L_3 edge or the antiferromagnetic Cr L_3 edge. The ferromagnetic domain pattern is similar to the ones previously reported for Co/Pt multilayers, and the ferromagnetic and antiferromagnetic domains are spatially coupled. The magnetization curve measured after cooling the sample, while maintaining the demagnetized state, exhibited positive and negative exchange biases simultaneously, which suggests that the exchange bias is determined on a domain-by-domain basis.

Keywords: magnetic domain; antiferromagnet; exchange bias; focused soft X-ray; soft X-ray magnetic circular dichroism; soft X-ray absorption; microspectroscopy; fresnel zone plate

1. Introduction

Imaging of magnetic domains provides fundamental and essential information about magnetic properties such as the magnetization process and the spatial distribution of magnetic interactions [1].

Magnetic domains have been imaged by several microscopic techniques such as magnetic force microscopy [2], magneto-optic Kerr microscopy [3], and X-ray microscopy with dichroism [4,5]. While most techniques are applicable in the case of ferromagnetic (FM) materials, the direct observation of antiferromagnetic (AFM) domains is still a non-trivial matter because macroscopic magnetization is compensated in an antiferromagnet. Antiferromagnets have been extensively used in magnetoresistive devices in which the AFM layer is used to induce exchange bias [6,7,8], i.e. to fix the FM magnetization adjacent to the AFM layer in a certain direction [9]. The rather simple model proposed by the discoverers, Meiklejohn and Bean, overestimates the exchange bias field [6]; to solve this discrepancy, many models have been proposed in which the magnetic domain size and/or the motion of the AFM layer are taken into account [7,8,10,11,12]. Hence, we can access the central issue of the exchange bias by direct observation of FM and AFM domains and their coupling.

AFM domains have been imaged by means of element-specific microscopic techniques such as photoemission electron microscopy (PEEM) with X-ray magnetic linear dichroism (XMLD) [13–17]. Since XMLD does not require uncompensated AFM spins, this technique is applicable for the fully compensated AFM layer. While this technique is a powerful tool for the AFM domain imaging, sometimes the collinear spin configurations cannot be distinguished, depending on the electric field vector of the incident X-ray. This confinment is particularly serious for the perpendicular exchange-biased system, which is required for spintronic devices with low power consumption and high integration. In the simple perpendicular exchange-biased system, FM and AFM spins are restricted to up or down, and thus the spin configuration is always collinear. Nevertheless, this simple spin configuration is suitable for the investigation of the coupling between FM and AFM domains. In order to access this simple spin configuration, X-ray magnetic circular dichroism (XMCD) and XMLD are used in a complementary way.

In our previous paper [18], we reported that this simple spin configuration is realized in the Pt/Co/Cr_2O_3/Pt perpendicular exchange-biased system, which can be a model system for the above investigation. Furthermore, the perpendicular exchange bias of this system is controllable by an electric field via the magneto-electric effect of Cr_2O_3 [19,20,21], and it was predicted that AFM domain wall propagation dominates the switching process of the perpendicular exchange bias [21,22]. Hence, direct observation of the AFM domain in this system provides important information to understand the detailed mechanism of the electric control of the perpendicular exchange bias. However, up to now, the AFM domain and the coupling between FM and AFM domains in this system have not been imaged directly. In this study, we imaged both FM and AFM domains in Pt/Co/Cr_2O_3/Pt thin films exhibiting perpendicular exchange bias and investigated their coupling by means of soft X-ray microscopy combined with X-ray magnetic circular dichroism (XMCD).

2. Materials and Method

A Pt(1.5)/Co(0.5)/Cr_2O_3(100)/Pt(20) film (where the numbers in parentheses represent the thicknesses of the layers in nanometers) was prepared on an α-Al_2O_3(0001) substrate, using a DC magnetron sputtering system with a base pressure below 5×10^{-6} Pa. First, the 20-nm-thick Pt buffer layer was deposited on the substrate at room temperature and was annealed for 30 minutes at 673 K to smooth the surface. The Cr_2O_3 layer was deposited on top of the Pt buffer layer at 773 K by reactive sputtering, using an Ar and O_2 gas mixture. The Co and Pt layers were prepared at room temperature. The gas pressure was maintained at 0.5 Pa during deposition of the Pt and Cr_2O_3 layers

and at 0.6 Pa during deposition of the Co layer. These procedures yielded a crystalline orientation normal to the film in the Pt(111), Cr_2O_3(0001), and Co(111) films. The details of the preparation conditions and crystalline quality of the sample may be referenced in our previous paper [18].

Prior to performing the XMCD measurements, we determined the magnetic easy-axis direction of the fabricated film. Figure 1 shows the magnetization curves measured by the vibrating sample magnetometer (VSM) and the polar magneto-optic Kerr effect (MOKE) measurement system. Note that, because the FM layer thickness of our sample was only 0.5 nm, the magnetization value was close to the sensitivity limit of the VSM, and thus in order to detect the magnetization signal with a high sensitivity, the polar MOKE system was also used (blue line in Figure 1). When the magnetic field was applied perpendicular to the film, the magnetization saturated easily, and the resulting remanent magnetization is high. On the other hand, the magnetization increases linearly with an in-plane magnetic field; both the remanent magnetization and coercivity are zero. This means that the film exhibits perpendicular magnetic anisotropy (PMA), in agreement with our previous results [23]. The XMCD imaging and spectrum measurements described below were performed after the sample had been demagnetized by application of an AC magnetic field perpendicular to the film.

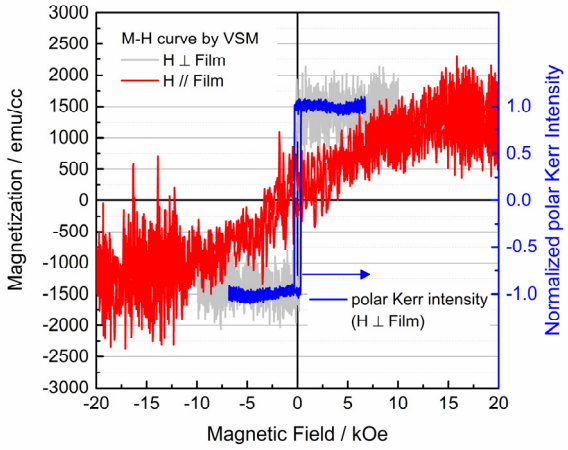

Figure 1. Magnetization curves of Pt(1.5)/Co(0.5)/Cr_2O_3(100)/Pt(20)/substrate. Magnetizations measured by the vibrating sample magnetometer (gray and red curves) are shown on the left axis, and the polar Kerr signal (blue) is shown on the right axis. The applied field direction was parallel (red) or perpendicular (gray, blue) to the film plane.

The absorption and XMCD measurements were performed at the BL25SU beamline of the SPring-8 synchrotron radiation facility. The optical and measurement setups are shown schematically in Figure 2. The BL25SU beamline is equipped with twin helical undulators, in which the circularly polarized soft X-rays are generated, and the helicity can be switched periodically by kicker magnets [24]. The XMCD intensity is proportional to the projection of the magnetization onto the direction of photon propagation, and the fabricated film exhibits PMA (Figure 1). In this work, to accurately detect the tiny XMCD signal from the AFM spins, the soft X-ray beam was incident along the direction normal to the film. Note that it is sometimes difficult to achieve the normal incidence of the X-ray in a conventional PEEM setup.

To image the magnetic domains based on the XMCD measurements, we used focused soft X-rays. The emitted soft X-ray was focused on the sample by a Fresnel zone plate (FZP) and an order-sorting aperture (OSA). In this setup, the spot size of the focused soft X-ray beam, estimated by a knife-edge method, is less than 100 nm. The details of the optical and measurement setup will be described elsewhere [25]. In measurement systems using focused soft X-rays, the transmission configuration is often adopted [5,26–29] while the total electron yield (TEY) method is also applicable [30]. In our experiment, the TEY method was employed to detect the soft X-ray absorption in order to ensure surface sensitivity [16,31,32]. To utilize the TEY method, a bias voltage of −18 V was applied to the sample. Using this setup, we performed two types of measurements: one involved imaging of the spatial distributions of the soft X-ray absorption and XMCD, and the other involved measuring the soft X-ray absorption (XAS) and XMCD spectra. For these two types of measurements, the scanning axes were altered as shown in Table 1. For the imaging experiments, the helicity of the incident X-rays was fixed as positive (μ_+) or negative (μ_-), and the z positions (the incident X-ray orientation) of the OSA and sample were also fixed at the focused conditions. With this configuration, the sample was scanned in the x-y plane to image the spatial distribution of the absorption. In the present study, two scanning modes were adopted depending on the signal intensity: the step scan and the continuous scan. In the step scan mode, the x and y motions were temporary stopped and the signal was accumulated during the sampling time. The continuous scan mode is usually used in scanning probe microscopy studies; in this mode, the sample was continuously moved along the x direction line by line. While the image acquisition time depends on the scan conditions, i.e. the scan step, the scan speed, the line step, and the sampling time, it was typically about 1000 seconds. For the spectroscopy experiments, the helicity of the incident X-rays was switched at a frequency of 1 Hz by the kicker magnets of the twin helical undulators. The soft X-rays were made to irradiate a fixed point on the sample by maintaining the x and y positions. To retain the focused conditions while the photon energy was changing, the z positions of the OSA and sample were adjusted, synchronized with the photon energy, so that the A/B value would remain constant (see Figure 2). The XCMD signals were obtained by calculating the difference between the absorptions corresponding to the positive and negative incident X-ray helicities, $\mu_+ - \mu_-$, while for XMCD mapping, the XMCD signals were normalized by the absorption, $(\mu_+ - \mu_-)/(\mu_+ + \mu_-)$.

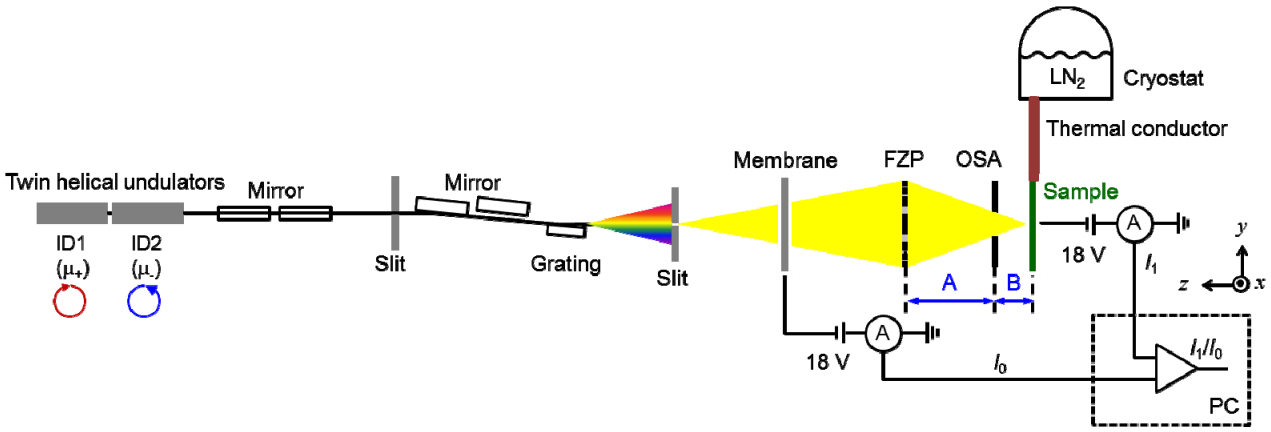

Figure 2. Schematic drawing of optical and measurement setups.

It is known that the Néel temperature of bulk Cr_2O_3 is 307 K [33] and that it can decrease in the case of thin films. We previously reported that the Néel temperature of the Cr_2O_3 thin film was near 285 K, which is below room temperature [21]. Thus, in our experimental setup (Figure 2), the sample was cooled via a thermal conductor, which connected the sample to a cryostat filled with liquid nitrogen. Because the lowest accessible sample temperature in this setup was 205 K, the magnetic domain observations were performed at room temperature (~ 295 K) and at 205 K.

Table 1. Scanning axes for absorption/XCMD imaging and spectroscopy.

	Helicity	***x*, *y* axes**	***z* axis**
Imaging	Fixed	Scanned	Fixed
Spectroscopy	Switched at 1 Hz	Fixed	Adjusted according to the photon energy to maintain the A/B ratio constant

3. Results and Discussion

3.1. Magnetic domain imaging and spectroscopy using focused soft X-rays

Before showing the results of FM and AFM domain observations, we show the instrumental capability because magnetic domain imaging based on XMCD measurements using focused X-rays—in particular with the TEY method—has been reported in very limited case [31,32]. Figure 3 shows the spatial distribution of the soft X-ray absorption measured at a photon energy of 778 eV, Co L_3-edge. The energy resolving power $E/\Delta E$ is 1250. The measurements were performed at room temperature. The images were obtained by the step scan mode with 400 nm steps, and the total number of pixels was 151 × 151. The sampling time per pixel was 0.05 sec. Note that, in the images shown in Figure 3, no contrast adjustment and no background correction were applied; the contrast was simply maximized using the maximum and minimum values of each image.

Clear contrast is observed in this image, which was obtained by using incident X-rays with fixed helicities. When the helicity is switched, the observed contrast is reversed as can be clearly seen by comparing Figs. 3(a) and 3(b). If the observed contrast originates from the compositional distribution, it should be independent of the helicity of the incident X-rays. Thus, the reversal of the contrast indicates that the observed contrast is generated by the XMCD. Besides, the contrast vanished in the summed image of μ_+ and μ_-, Figure 3(c) and the image is rather homogeneous, which is reasonable because Figure 3(c) provides the spatial distribution of the chemical composition of Co that was deposited homogeneously. The weak contrast in Figure 3(c) may be due to the burn-in of contaminants such as carbon that adhered to the sample in the atmosphere before it was introduced into the XMCD chamber, or to an artefact caused by the measurement setup, in which the incident X-ray intensity I_0 was measured before the FZP, whereas the generated current I_1 was measured after the FZP (see Figure 2). The difference between Figs. 3(a) and 3(b) provides the spatial distribution of the XMCD. The observed pattern is similar to the magnetic domain pattern observed by the MOKE microscope (Figure 3(e)); the image shown in Figure 3(d) corresponds to the magnetic domain pattern. In Figure 3(d), the red and blue regions indicate magnetic domains with down and up

magnetizations, respectively. The magnetic domain pattern is similar to that observed in a Co(0.6)/Pt(2.0) multilayer on an AFM IrMn layer [36] and in antiferromagnetically coupled Co(0.4)/Pt(0.5) multilayers [37]. The dark curved line in Figure 3(c) and the white line in Figure 3(d) may be caused by structural defects such as a grain boundary because these lines are also observed in both the MOKE microscope image (Figure 3(e)) and in an optical microscope image (not shown). Compared with Figs. 3(d) and 3(e), we cannot recognize the clear signature of the image drift in the XMCD image despite the fact that the data acquisition times are highly different for the two measurements: about an hour for Figure 3(d) and a few minutes for Figure 3(e). Thus, it is likely that the thermal drift during the imaging is negligibly small.

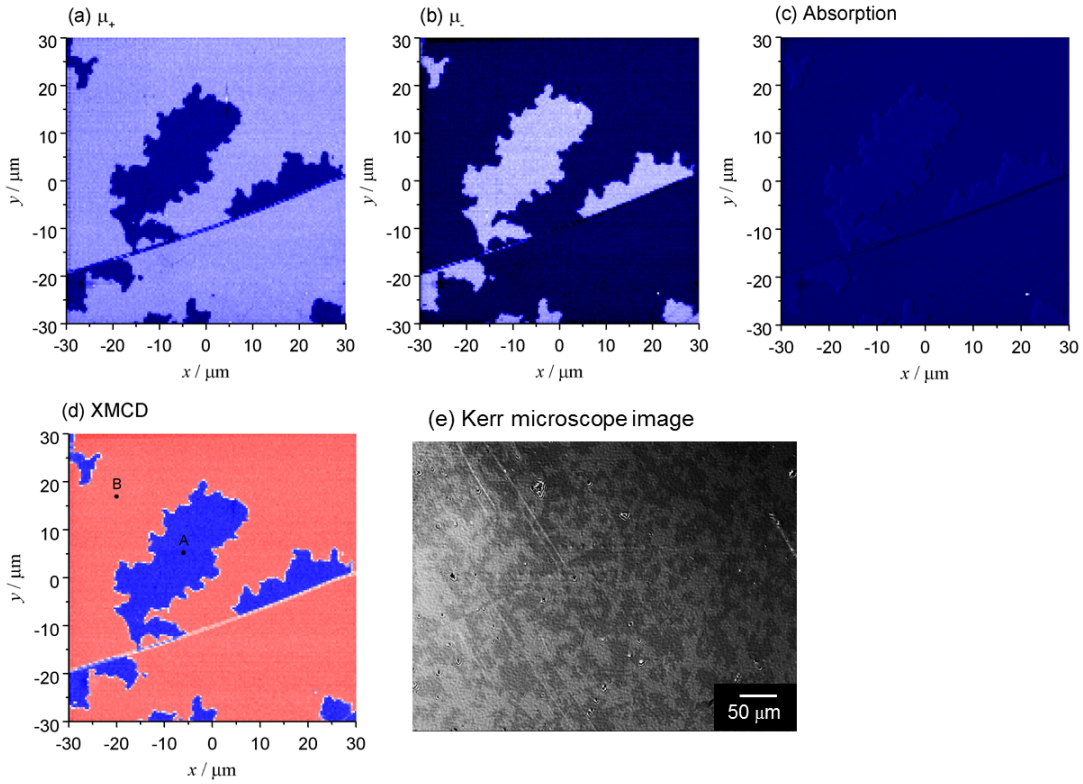

Figure 3. Spatial distribution of soft X-ray absorption at a photon energy of 778 eV, Co L_3-edge. The helicity of the soft X-rays was maintained as (a) positive μ_+ and (b) negative μ_- during the measurements. (c) and (d) represent summation, $\mu_+ + \mu_-$, and normalized difference, $(\mu_+ - \mu_-)/(\mu_+ + \mu_-)$, respectively, of (a) and (b); these correspond to the spatial distribution of total absorption and XMCD, respectively. Dark blue and light blue contrasts in (a) and (b) represent the high and low absorption intensity, respectively. Red and blue contrasts in (d) represent the positive and negative XMCD, respectively. Spectra were measured at positions denoted as A and B in (d) (see Figure 4). (e) Magnetic domain image observed by the MOKE microscope.

In order to further ensure that the observed contrast is generated by the XMCD, the XAS and XCMD spectra were measured on the oppositely directed magnetic domains, at the specific

positions denoted as A and B in Figure 3(d). Figure 4 shows the measured spectra, and both XAS and XMCD spectra were successfully obtained, which ensures that the observed contrast shown in Figure 3(d) originated from the magnetic domains. The accuracy of the *x* and *y* positions was about 500 nm. Ideally, the accuracy of the *x* and *y* positions is comparable to the spot size of the focused X-ray, but in actuality, it was restricted by the disturbance of the *x* and *y* positions that occurred while moving the sample in the *z* direction to maintain the focused condition during the photon energy change. Besides, the effective spin moment m_{s_eff} and the orbital moment m_{orb} can be estimated from these spectra by sum rule analysis [38,39]. However, the integration range of the photon energy, from 770 eV to 810 eV is insufficient for the precise estimation of m_{s_eff} and m_{orb}; the insufficient integration range tends to overestimate m_{orb}/m_{s_eff} [29]. In addition, the degree of circular polarization after passing through the FZP is unknown; comparing the XAS and XMCD spectra with the reference spectrum (for example, Figure 1 of reference 21), the degree of circular polarization is likely to be comparable to that of the un-focused soft X-ray before transmission of FZP, 0.96 [40]. Nevertheless, further investigation will be required to determine this precise value, which is beyond the scope of this paper.

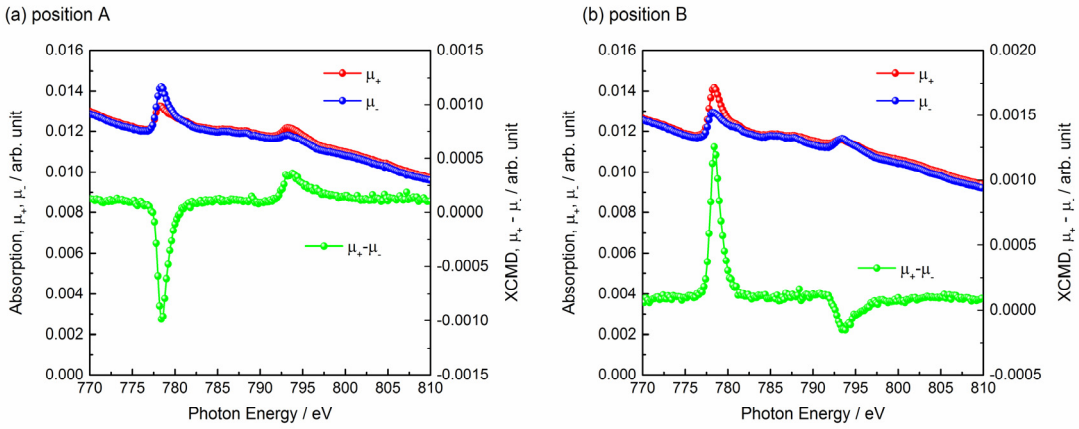

Figure 4. Absorption and XMCD spectra measured at Co $L_{2,3}$-edges. Measurements were performed at positions (a) A and (b) B shown in Figure 3(d) while maintaining the focused state of the soft X-ray beam. These spectra were collected by switching helicity at a frequency of 1 Hz.

3.2. Spatial coupling between FM and AFM domains

FM and AFM domains were observed at the photon energy of 778 eV (Co L_3 edge) and 576 eV (Cr L_3 edge), respectively. Note that the XMCD signal from the AFM spins is generated from the interfacial uncompensated spins probably caused by the equilibrium boundary magnetization on the $Cr_2O_3(0001)$ surface [34,41,42] that are exchange-coupled with the FM spins. Figure 5 shows the spatial distributions of XMCD corresponding to FM and AFM domains. The images shown in (a) and (b) were collected by the step scan mode with 500–600 nm steps and those shown in (c) and (d) were produced by the continuous scan mode with the scan speed of 6–12 μm/s and line steps of 200–300 nm. Even at the Cr L_3 edge, the magnetic domain patterns were successfully observed. It can be seen that the contrasts at Co L_3 an Cr L_3 edges are reversed with respect to each other; this is

due to the antiferromagnetic coupling between Co and interfacial uncompensated Cr spins [18]. It is surprising that the XMCD contrast at Cr L_3 edge is observable at room temperature, above the Néel temperature of the Cr_2O_3 thin film. This implies that short-range order is induced in the Cr_2O_3 layer in the vicinity of the Co/Cr_2O_3 interface by the interfacial exchange coupling. The observed domain at Cr L_3 edge pattern is similar to that of the FM domain, which indicates that these domains are coupled. At room temperature, the boundary of the oppositely directed magnetic domain is not sharp (Figure 5(b).) because the XMCD signal from the induced Cr spins is very weak. The AFM domain becomes clear below the Néel temperature, and the AFM domain pattern is still same as the FM domain pattern (Figure 5(c) and (d)). This is explained by the AFM domain formation process. As mentioned above, the Néel temperature of the Cr_2O_3 thin film is below the deposition temperature of Co. In this case, when the FM domains are formed, Cr_2O_3 is still paramagnetic although it is likely that the induced spins in the Cr_2O_3 layer at the interface to Co already exist because of the short-range-order in the vicinity of the interface. Because this short-range-order was designated as the starting point for the long-range AFM order parameter, the magnetic domain pattern observed at room temperature persisted below the Néel temperature.

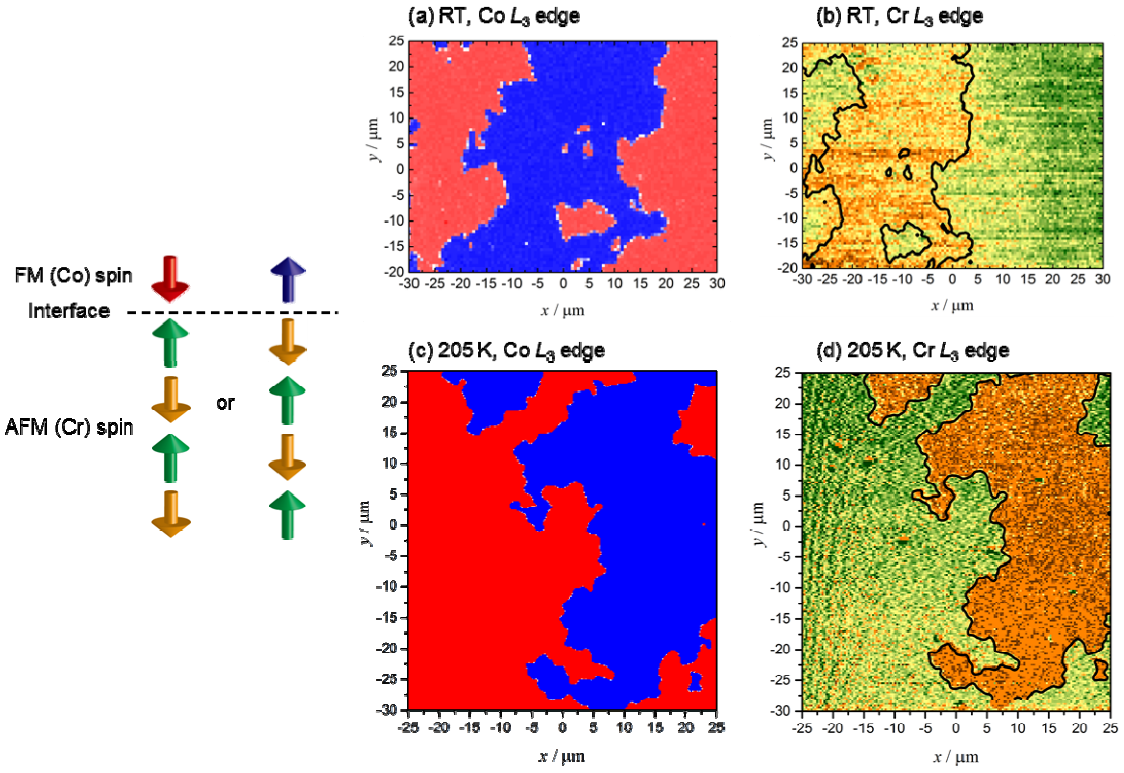

Figure 5. Spatial distribution of XMCD measured at (a), (b) room temperature and (c), (d) 205 K. Photon energy used for the imaging was (a), (c) 778 eV (Co L_3 edge) and 576 eV (Cr L_3 edge). Measurements were carried out in the AC-demagnetized state. Black solid lines in (b) and (d) represent the domain boundary of the oppositely directed FM domains. Red and blue contrast in (a) and (c) represents the positive and negative XMCD meaning that red and blue contrasts are generated by the down and up Co spins, respectively. Orange and green contrast was induced by the down and up uncompensated Cr spins as shown in a left schematic drawing.

Matching of FM and AFM domain patterns is different from the situation with in-plane exchange biased systems such as Co/NiO [13] and Co/$LaFeO_3$ [15] in which multi-FM domains were observed on the individual AFM domains. This difference may be due to the allowable spin configuration and the detection technique of AFM spins: XMLD or XMCD. In the in-plane exchange-biased systems, the magnetic easy direction is typically fourfold symmetric in the film plane and both FM and AFM spins can be oriented along the $\pm x$ and $\pm y$ directions. In this spin configuration, when the electric field vector of the incident X-ray lies in the film plane, the two domains with collinear in-plane projection cannot be distinguished by XMLD [13,15]; for example, the AFM spins pointing to the $\pm x$ directions generate the same magnetic contrast. In our system, as shown in Figure 1, the FM layer exhibits PMA which restricts the FM spin orientation to the $\pm z$ directions, and the AFM spins are also restricted to up or down, the $\pm z$ directions [18] owing to the magnetocrystalline anisotropy and the crystallographic orientation of the Cr_2O_3 layer [43]. In our experiment, the soft X-ray beam was incident from the surface normal, and in this geometry, the collinear spin configurations are distinguishable by XMCD. Hence, the results shown in Figure 5 provide direct evidence that the FM and AFM domain patterns are fully coupled. The coincidence of FM and AFM domain patterns suggests that the interfacial exchange coupling dominates the AFM domain pattern.

We further investigate the coupling of FM and AFM domains using the magnetization curve. Figure 6 shows the polar MOKE loops measured at 141 K after zero-field cooling (ZFC). Before the ZFC, the sample was demagnetized by an AC magnetic field, i.e. the sample was cooled while maintaining the demagnetized state. In the magnetization curve, the positive and negative exchange biases were observed simultaneously. The exchange bias fields are same for the positive and the negative biases, and these values are identical to that measured after the field-cooling (see inset of Figure 6). Among many models of the exchange bias, some models predict that the local exchange bias fields are inversely proportional to the in-plane AFM domain size [44]. While the magnetic domain sizes in our films are not especially uniform, as seen in Figs. 3 and 5, the above coincidence of the exchange bias fields implies that the in-plane AFM domain model may not be available for our system. This is because the underlying idea of the above model is that the uncompensated AFM spins are induced by structural defects—for example, by interface roughness—and the width of the exchange bias distribution is proportional to the uncompensated AFM spin per unit area [11,12]. In contrast, the interfacial uncompensated AFM spins in Pt/Co/Cr_2O_3 thin films are the result of the roughness-insensitive equilibrium boundary magnetization of the Cr_2O_3(0001) surface [19,34,42] and the amount of the uncompensated AFM spin is independent of the exchange bias field [34]. In this case, the AFM domain pattern mimics the FM domain pattern via the interfacial exchange coupling, especially when the film was cooled from above the Néel temperature. Then the exchange bias is explained by the formation of the magnetic domain wall structure in the AFM layer as proposed by Mauri et al. [10]. In this manner, the local exchange bias can be determined on a domain-by-domain basis. The values of P and N displayed in the main part of Figure 6 reflect the area ratio exhibiting the positive and the negative exchange biases, respectively, within the probed area. The reason why the values of P and N are not equal is probably that the diameter of the probe laser used in the MOKE instrument was below 0.1 mm, with the result that the probed areas of magnetic domains with up and down magnetization were not equal.

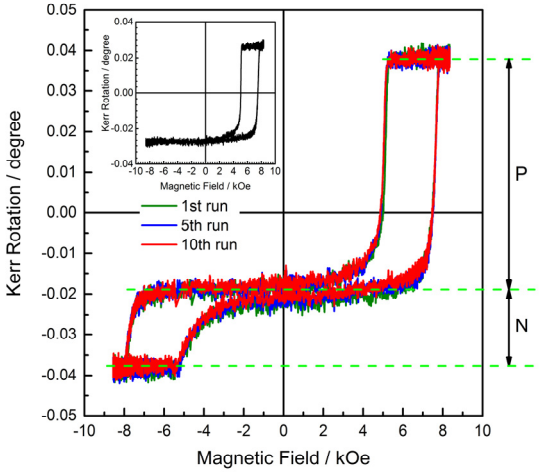

Figure 6. Magnetization curves of the studied film, Pt(1.5)/Co(0.5)/Cr_2O_3(100)/Pt(20)/substrate measured at 141 K after zero-field cooling. Green, blue and red lines represent curves for the 1st, 5th and 10th magnetic-field cycles, respectively. The inset shows the magnetization curve measured after cooling in a constant field of −4 kOe.

The magnetization curve shown in Figure 6 also provides the stability of the magnetic domain pattern. In the exchange-biased system, a training effect of the exchange bias, i.e. a reduction of the exchange-bias field after repeated magnetic field cycling [7,8] sometimes occurs, and is explained by the rearrangement of the AFM domain structure with each FM spin reversal [45]. As shown in Figure 6, neither the positive nor the negative exchange-bias field changes with the number of magnetic field cycles; the training effect is absent. The absence of the training effect implies that AFM domain patterns are stable under FM spin reversal, and this result also agrees with the prediction that the interfacial uncompensated AFM spins are caused by the equilibrium boundary magnetization, and the exchange bias is produced by individual AFM domains.

4. Conclusion

The FM and AFM domains in Pt/Co/Cr_2O_3/Pt thin film were separately observed by XMCD measurements using a focused soft X-ray beam. The AFM domain patterns were same as the FM domain patterns, which means that the two types of domains are coupled. The magnetization curve after cooling the sample while maintaining the demagnetized state exhibited the positive and negative exchange biases simultaneously. Moreover, the training effect on the exchange bias was absent for both the positive and the negative exchange biases, indicating that the rearrangement of the magnetic domain structure is negligible. These results suggest that the exchange bias was induced on a domain-by-domain basis.

Acknowledgments

Author (Y.S) thanks Dr. Takuo Ohkochi for the help with the magnetic domain observation using the Kerr microscope. The XAS and XMCD experiments were performed at the SPring-8

synchrotron radiation facility with the approval of JASRI (Proposal Nos. 2014A0079, 2014B0079 and 2015A0079). This work was partly supported by JSPS KAKENHI Grant No. 25706007, the ImPACT program of the Council for Science, Technology and Innovation (Cabinet Office, Government of Japan), and the Photonics Advanced Research Center (PARC) at Osaka University.

Conflict of Interest

The authors report no conflict of interests in this research.

References

1. Hubert A, Schäfer R (2000) Magnetic Domains, New York, Springer, 395–520.
2. Wiesendanger R (1994) Scanning Probe Microscopy and Spectroscopy, Cambridge, Cambridge Press, 251–264.
3. MacCord J (2015) Progress in magnetic domain observation by advanced magneto-optical microscopy. *J Phys D Appl Phys* 48:333001.
4. Spanke D, Dresselhaus J, Kinoshita T, et al. (1996) Element-specific magnetic domain imaging based on linear and circular magnetic dichroism in photoabsorption. *J Electron Spectrosc Relat Phenom* 78: 299–302.
5. Fischer P, Kim DH, Mesler BL, et al. (2007) Exploring nanomagnetism with soft X-ray microscopy. *Surf Sci* 601: 4680–4685.
6. Meiklejohn WH, Bean CP (1957) New magnetic anisotropy. *Phys Rev* 105: 904–913.
7. Nogués J, Schuller IK (1999) Exchange bias. *J Magn Magn Mater* 192:203–232.
8. Berkowitz AE, Takano K (1999) Exchange anisotropy – a review. *J Magn Magn Mater* 200: 552–570.
9. Dieny B, Speriosu VS, Parkin SSP, et al. (1991) Giant magnetoresistive in soft ferromagnetic multilayers. *Phys Rev B* 43: 1297–1300.
10. Mauri D, Siegmann HC, Bagus PS, et al. (1987) Simple model for thin ferromagnetic films exchange coupled to an antiferromagnetic substrate. *J Appl Phys* 62: 3047–3049.
11. Malozemoff AP (1987) Random-field model of exchange anisotropy at rough ferromagnetic-antiferromagnetic interface. *Phys Rev B* 35: 3679–3682.
12. Malozemoff AP (1988) Mechanisms of exchange anisotropy (invited). *J Appl Phys* 63: 3874–3879.
13. Duò L, Finazzi M, Ciccaci F (2010) Magnetic properties of antiferromagnetic oxide materials. Weinheim: Wiley-VCH, 301–339.
14. Scholl A, Stöhr J, Lüning J, et al. (2000) Observation of antiferromagnetic domains in epitaxial thin films. *Science* 287: 1014–1016.
15. Nolting F, Scholl A, Stöhr J, et al. (2000) Direct observation of the alignment of ferromagnetic spins by antiferromagnetic spins. *Nature* 405: 767–769.
16. Ohldag H, Regan TJ, Stöhr J, et al. (2001) Spectroscopic identification and direct imaging of interfacial magnetic spins. *Phys Rev Lett* 87: 247201.
17. Arai K, Okuda T, Tanaka A, et al. (2012) Three-dimensional spin orientation in antiferromagnetic domain walls of NiO studied by X-ray magnetic linear dichroism photoemission electron microscopy. *Phys Rev B* 85: 104418.

18. Shiratsuchi Y, Noutomi H, Oikawa H, et al. (2012) Detection and in situ switching of unreversed interfacial antiferromagnetic spins in a perpendicular-exchange-biased system. *Phys Rev Lett* 109: 077202.
19. He X, Wang Y, Wu N, et al. (2010) Robust isothermal electric control of exchange bias at room temperature. *Nature Mater* 9: 579–585.
20. Ashida T, Oida M, Shimomura N, et al. (2015) Isothermal electric switching of magnetization in Cr_2O_3/Co thin film system. *Appl Phys Lett* 106: 132407.
21. Toyoki K, Shiratsuchi Y, Kobane A, et al. (2015) Magnetoelectric switching of perpendicular exchange bias in Pt/Co/α-Cr_2O_3/Pt stacked films. *Appl Phys Lett* 106: 1624004.
22. Martin T, Anderson JC (1966) Antiferromagnetic domain switching in Cr_2O_3. *IEEE Trans Magn* 2: 446–449.
23. Shiratsuchi Y, Oikawa H, Kawahara S, et al. (2012) Strong perpendicular magnetic anisotropy at Co(111)/α-Cr_2O_3(0001) interface. *Appl Phys Express* 5: 043004.
24. Muro T, Nakamura T, Matsushita T, et al. (2005) Circular dichroism measurement of soft X-ray absorption using helicity modulation of helical undulator radiation. *J Electron Spectrosc Relat Phenom* 144–147: 1101–1103.
25. Kotani Y et al. in preparation.
26. Fischer P, Eimüller T, Schütz G, et al. (1999) Magnetic domain imaging with a transmission X-ray microscope. *J Magn Magn Mater* 198–199: 624–627.
27. Fischer P, Fadley CS (2012) Probing nanoscale behavior of magnetic materials with soft X-ray spectromicroscopy. *Nanotechnol Rev* 1: 5–15.
28. Ohtori H, Iwano K, Mitsumata C, et al. (2014) Visualization of magnetic dipolar interaction based on scanning transmission X-ray microscopy. *J Phys Conf Series* 502: 012010.
29. Robertson MJ, Agostino CJ, N'Diaye AT, et al. (2015) Quantitative x-ray magnetic circular dichroism mapping with high spatial resolution full-field magnetic transmission soft x-ray spectro-microscopy. *J Appl Phys* 117: 17D145.
30. Kim GB, Song HJ, Shin HJ, et al. (2005) X-ray absorption spectroscopy in total electron yield mode of scanning photoelectron microscopy. *J Electron Spectrosc Relat Phenom* 148: 137–141.
31. Nolle D, Weigand M, Schütz G, et al. (2011) High contrast magnetic and nonmagnetic sample current microcopy for bulk and transparent sample using soft X-rays. *Microsc Microanal* 17: 834–842.
32. Nolle D, Weigand M, Audehm P, et al. (2012) Note: Unique characterization possibilities in the ultra high vacuum scanning transmission x-ray microscope (UHV-STXM) "MAXYMUS" using a rotatable permanent magnetic field up to 0.22 T. *Rev Sci Instrum* 83: 046112.
33. Nakajima R, Stöhr J, Idzerda YU (1999) Electron-yield saturation effects in *L*-edge x-ray magnetic circular dichroism spectra of Fe, Co, and Ni. *Phys Rev B* 59:6421–6429.
34. Toyoki K, Shiratsuchi Y, Nakamura T, et al. (2014) Equilibrium surface magnetization of α-Cr_2O_3 studied through interfacial chromium magnetization in Co/α-Cr_2O_3 layered structures. *Appl Phys Express* 7: 114201.
35. Astrov DN (1961) Magnetoelectric effect in chromium oxide. *J Exptl Theoret Phys* 40: 1035–1041.
36. Ji X, Pakhomov AB, Krishnan KM (2007) Asymmetric magnetic reversal of perpendicular exchange biased $(Co/Pt)_5$/IrMn probed by magnetoresistance and magnetic force microscopy. *J Appl Phys* 101: 09E507.

37. Liu ZY, Li N, Zhang F, et al. (2008) Effect of magnetic field on domain-wall structures in two antiferromagnetically coupled Co/Pt multilayers. *Appl Phys Lett* 93: 032502.
38. Thole BT, Carra P, Sette F, et al. (1992) X-ray circular dichroism as a probe of orbital magnetization. *Phys Rev Lett* 68: 1943–1946.
39. Carra P, Thole BT, Altarelli M, et al. (1993) X-ray circular dichrosism and local magnetic fields. *Phys Rev Lett* 70: 694–697.
40. Oura M, Nakamura T, Takeuchi T, et al. (2007) Degree of circular polarization of soft X-rays emitted from a multi-polarization-mode undulator characterized by means of magnetic circular dichroism measurements. *J Synchrotron Rad* 17: 483–486.
41. Andeev AF (1996) Macroscopic magnetic fields of antiferromagnets. *J Exptl Theoret Phys* 63: 758–762.
42. Belashchenko KD (2010) Equilibrium magnetization at the boundary of a magnetoelectric antiferromagnet. *Phys Rev Lett* 105: 147204.
43. Corliss LM, Hastings JM, Nathans R, et al. (1965) Magnetic structure of Cr_2O_3. *J Appl Phys* 36: 1099–1100.
44. Scholl A, Nolting F, Seo JW, et al. (2004) Domain-size-dependent exchange bias in Co/$LaFeO_3$. *Appl Phys Lett* 85: 4085–4087.
45. Hoffmann A (2004) Symmetry driven irreversibilities at ferromagnetic-antiferromagnetic interfaces. *Phys Rev Lett* 93: 097203.

AIMS Press